

The Luminosity Function of X-ray Point Sources in Centaurus A

R. Voss and M. Gilfanov

Max Planck Institut für Astrophysik, Germany
email:[voss;gilfanov]@mpa-garching.mpg.de

Received ... / Accepted ...

Abstract. We have studied the X-ray point source population of Centaurus A (NGC 5128) using data from four archival *CHANDRA* observations. We detected 272 point-like X-ray sources within a radius of $10'$ from the centre. Approximately half of these are CXB sources, with the remaining half being LMXBs. The spatial distribution of the LMXBs, both azimuthally averaged and 2-D, is consistent with the distribution of the *K*-band light observed in the 2MASS survey. After correction for the incompleteness effect we constrain the LMXB luminosity function down to $\sim 2 \times 10^{36}$ erg s $^{-1}$, much lower than previous studies of LMXBs in elliptical galaxies. The obtained XLF flattens significantly below $L_X \sim 5 \times 10^{37}$ erg s $^{-1}$ and follows the $dN/dL \propto L^{-1}$ law in agreement with the behaviour found earlier for LMXBs in the Milky Way and in the bulge of M31.

Key words. galaxies: individual: Centaurus A, NGC 5128 – X-rays: binaries – X-rays: galaxies

1. introduction

CHANDRA observations of the bright end, $\log(L_X) \gtrsim 37.5 - 38$, of X-ray point source populations in nearby elliptical galaxies found a rather steep luminosity distribution with a differential power law index in the $\sim 1.8 - 2.5$ range (e.g. Colbert et al. 2004; Kim & Fabbiano 2004). This is noticeably steeper than X-ray luminosity function (XLF) slopes in spiral and starburst galaxies, ~ 1.6 (Grimm et al. 2003). This difference reflects the difference in the composition of the X-ray populations in the early and late type galaxies, dominated by low- and high-mass X-ray binaries, respectively. Extension of the luminosity range available for the study down to $\log(L_X) \sim 36$ revealed a much more complex shape of the XLF of low-mass X-ray binaries (LMXBs). It has been shown to flatten considerably at the faint end and to follow the $dN/dL \propto L^{-1}$ power law below $\log(L_X) \lesssim 37 - 37.5$ (Gilfanov 2004). Motivated by observational results, Bildsten & DeJoye (2004) and Postnov & Kuranov (2004) suggested that the slope of the LMXB XLF in different luminosity regimes is defined by predominantly different sub-types of low-mass X-ray binaries. In the sample of Gilfanov (2004) the faint end of the LMXB XLF was represented by the bulges of two spiral galaxies only – the Milky Way and M31. On the other hand, the X-ray binaries in the elliptical galaxies and spiral bulges could be formed by different mechanisms and have different evolution histories and, consequently, different luminosity distributions. It is, therefore, important to complement theoretical advances in understanding the XLF of X-ray binaries with firm observational constraints on its behaviour based on a broad range of the galactic types, especially at the low luminosity end.

Send offprint requests to: R. Voss

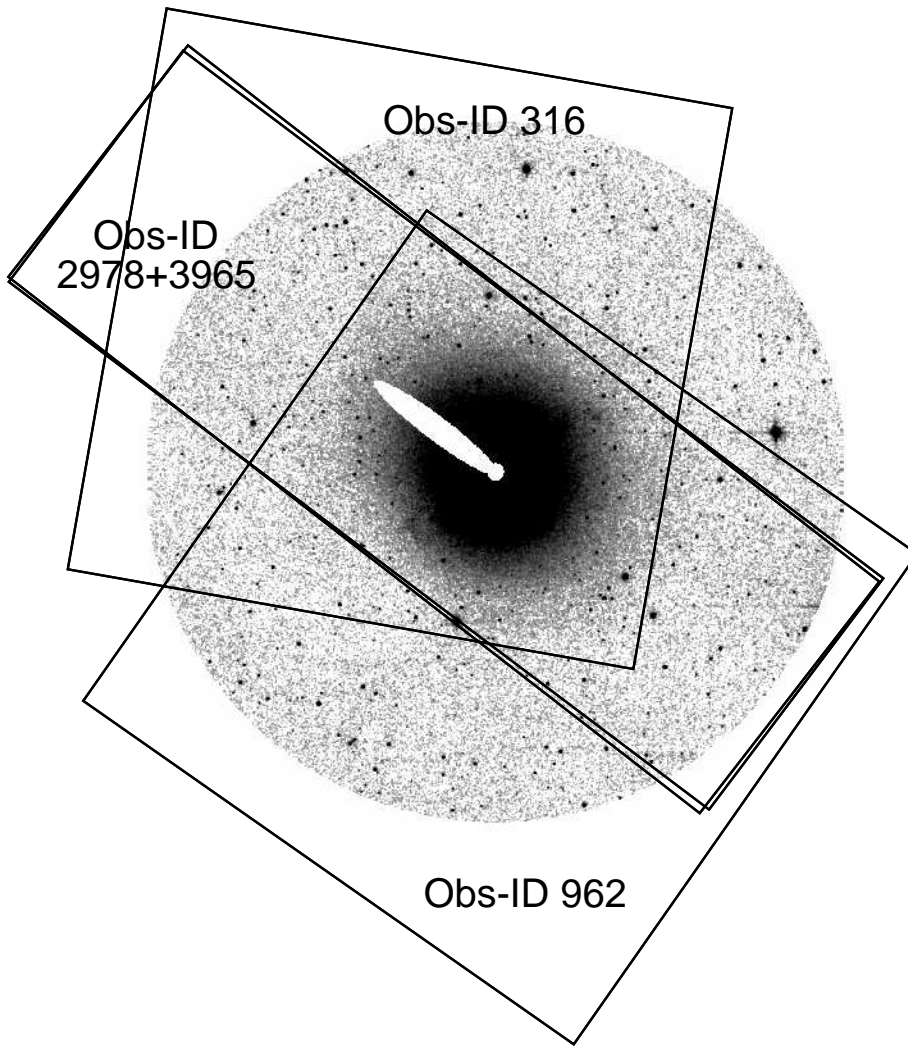
Centaurus A (Cen A) is the primary candidate for such a study. It is massive enough to contain sufficient number of LMXBs and, on the other hand, is sufficiently nearby to reach luminosities below $\sim 10^{37}$ erg s $^{-1}$ with moderate observing time. It has been widely studied in X-rays, and it has been observed 10 times with *CHANDRA*. These observations have been used to obtain information about the nucleus (Evans et al. 2004), the interstellar medium (Kraft et al. 2003), the jet (Kraft et al. 2002; Hardcastle et al. 2003) the shell structures (Karovska et al. 2002) and the off-centre point source population (Kraft et al. 2001). The objective of the present study is the population of LMXBs in Cen A, namely their spatial and luminosity distribution. Studying the latter, we will focus specifically on the low luminosity domain, $\log(L_X) \sim 36.5 - 37.5$, which importance has been emphasized above. Combining 4 observations and accurate incompleteness correction enabled us to investigate sources with luminosity by a factor of $\sim 5 - 10$ lower than in previous studies.

Cen A has a strongly warped dust disc with evidence for star formation, and optical images show a system of filaments and shells. This is probably due to a recent merger (Schiminovich et al. 1994). It is the nearest active galaxy and is considered to be the prototypical Faranoff-Riley class I radio galaxy. It has a very compact nucleus, most likely an accreting massive black hole, with strongly varying intensity. Emanating from this nucleus are milliarcsecond radio jets and a subrelativistic radio/X-ray jet is extending $\sim 6'$ towards NE of the nucleus. Also radio lobes extending NE and SW are seen. An exhaustive review of Cen A can be found in (Israel 1998).

The paper is structured as follows. In Sect. 2 we describe the data sets and the basic data preparation and analysis. The source list cleaning procedures are presented in Sect. 3, to-

Table 1. The *CHANDRA* observations used in this paper.

Obs-ID	Date	Instrument	Exp. Time	R.A.	Dec.	Data Mode
0316	1999 Dec 05	ACIS-I	36.18 ks	13 25 27.61	-43 01 08.90	FAINT
0962	2000 May 17	ACIS-I	36.97 ks	13 25 27.61	-43 01 08.90	FAINT
2987	2002 Sep 03	ACIS-S	45.18 ks	13 25 28.69	-43 00 59.70	FAINT
3965	2003 Sep 14	ACIS-S	50.17 ks	13 25 28.70	-43 00 59.70	FAINT

**Fig. 1.** The 2MASS *K*-band image of the region of Cen A analysed in this paper. The radius of the image is $10'$. Also shown are the areas covered by the four *CHANDRA* observations.

gether with source identifications. In this section we also deal with possible periodic variability of the most luminous sources. The properties of the population of X-ray binaries, as well as the background X-ray sources are analysed and compared with previous studies in Sect. 4, including the spatial distribution of the sources and their luminosity function. Sect. 5 gives the conclusions. We adopt a distance of 3.5 Mpc to Cen A, and that (R.A., Dec.) = (13 25 27.6, -43 01 08.8) is the centre of the galaxy.

2. Data Analysis

The analysis in this paper is based on four *CHANDRA* observations, two of them made with the ACIS-I array (OBS-ID 316 and 962), and the other two with the ACIS-S array (OBS-ID 2978 and 3965). Information about the observations is listed in Table 1, their fields of view overlaid on the *K*-band image of the galaxy are shown in Fig. 1.

Together these four observations cover most of Cen A within a $10'$ radius from the centre. The data preparation was

Table 2. The corrections applied to the *CHANDRA* aspect files to align the observations.

Obs-ID	Correction West	Correction North
0316	-0.73 pixel	-0.42 pixel
0962	+1.58 pixel	+1.44 pixel
2978	-0.53 pixel	-0.18 pixel
3965	-0.31 pixel	-0.85 pixel

done following the standard CIAO¹ threads (CIAO version 3.1; CALDB version 2.28), and limiting the energy range to 0.5–8.0 keV. The ACIS chips sometimes experience flares of enhanced background. For point source detection and luminosity estimation it is not necessary to filter out weak flares, since the increased exposure time outweighs the increased background. We did not find any flares strong enough to filter them out.

We used CIAO wavdetect to detect sources. This program is the most widely used for point source detection in *CHANDRA* data. Some of the parameters we have changed from the default values. Most important are the scales. We have used the $\sqrt{2}$ -series from 1.0 to 8.0. This gives a wide enough range of source sizes to account for the variation in point spread function (PSF) from the inner parts of Cen A to the parts 10' from the centre as well as enough middle scales. We also used maxiter=10, iterstop=0.00001 and bkgsigthresh=0.0001. The effect of changing these parameters is that more iterations are done in the process of removing sources when creating background files, at the expense of computing time. Finally we set the parameter eenergy=0.8 (the encircled fraction of source energy used for source parameter estimation), which gives larger areas for source parameter estimation at the risk of source merging, see Sect. 3.

First we detected sources in the inner region of Cen A covered by all four observations. From these sources we then chose 40 that are bright enough to have the positions determined precisely and existed in all four observations. We used these sources to determine the average positions of the sources and the offsets for the individual observations. The statistical uncertainties of the source positions are typically 0.3–0.5 pixel. Assuming that the errors are uncorrelated gives an uncertainty of ~ 0.05 pixel in the calculated offsets of the observations. Using CIAO dmcalc we then corrected the aspect and events file for each observation. The corrections applied are listed in Table 2. This step was performed in order to make the observations aligned for combination, not to get better absolute astrometry, which will be dealt with in Sect. 3.

We used CIAO reproject_events to reproject observations 316, 962 and 2978 into the sky coordinates of observation 3965. The files were then merged and the wavdetect task was applied again to the combined image. The output count rate for each detected source is calculated inside a source cell and the local background is subtracted. For each source we extracted the PSF using CIAO psfextract task and calculated the percentage of the counts expected to lie inside each source cell. This

was done for each of the four observations, and the result was averaged using the values of the exposure maps as weights. For most sources this percentage is above 97 per cent, and only four sources have values lower than 70 per cent. An exposure map was created for each of the observations, assuming the energy distribution to be a powerlaw with photon index of 1.7 and Galactic absorption of $8.4 \times 10^{20} \text{ cm}^{-2}$ (Dickey & Lockman 1990). We assumed the same spectrum to convert the observed count rates to unabsorbed source luminosities.

In the very inner parts of Cen A there is strong X-ray emission from hot gas and the central AGN. At the same time there is a large number of point sources within a small area making crowding a serious problem. We have therefore excluded the area within a radius of 30 pixels ($\sim 15''$) from the centre of the galaxy. Also the part of the galaxy dominated by the X-ray jet has been excluded. The excluded regions are evident from Fig. 1.

In each of the four observations, readout streaks caused by the bright central region of Cen A are seen. As in different observations they cover different regions of the image, for each streak we have searched for sources and estimated their parameters using a combined image of the observations, excluding the one containing this streak.

To check for differences between the four observations and between the individual observations and the combined observation, we have created the cumulative point source luminosity function for each, taking only sources from the central region, where all four observations overlap, see Fig. 1. The results can be found in Fig. 2. A large fraction of the sources are variable. For these sources, using the luminosities estimated from the combined image is equal to using the average luminosities. We used the Kolmogorov–Smirnov (KS)-test to compare the $\log(N) - \log(S)$ distribution obtained in the individual observations with that based on the combined data. To minimize incompleteness effects only sources with fluxes higher than $3 \cdot 10^{-15} \text{ erg s}^{-1} \text{ cm}^{-2}$ were used. The lowest found probability was 68 per cent (for Obs-ID 316). This confirms that the source variability does not modify the flux distribution of the point sources in a galaxy like Cen A on the detectable level.

3. The source list

Several effects can compromise the source list generated from CIAO wavdetect. Firstly, it is extended sources and false sources due to background fluctuations. The background due to the diffuse emission is high, especially in the inner parts of Cen A, and a lot of structures can be seen in the image. The “bubble” $\sim 5'$ south-west of the centre is one of the examples (Kraft et al. 2003). Some of these structures might be misinterpreted as point sources. We have visually inspected the images and for each source compared the photon distribution with the distribution expected from the PSF. As a result of this procedure we have rejected 18 sources. As indicated by the shape of their spectra, none of the rejected sources is likely to be a supernova remnant. Some of the rejected sources are filamentary structures in the diffuse component and the rest are false detections caused by local variations in the emission of the diffuse component.

¹ <http://cxc.harvard.edu/ciao/>

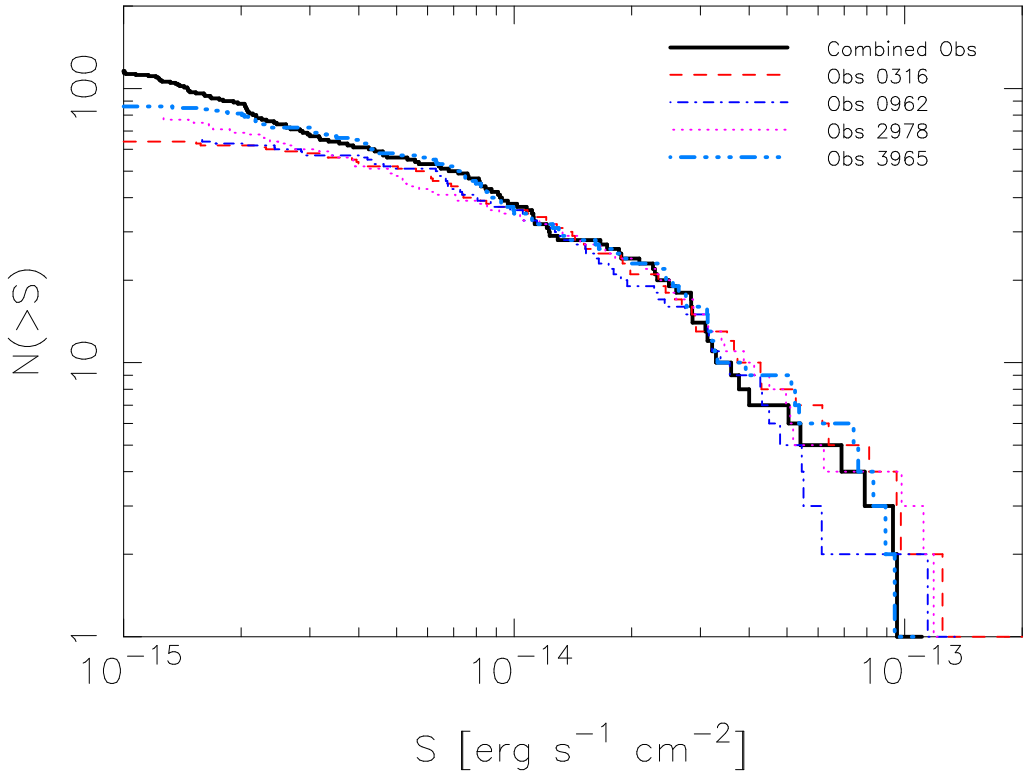


Fig. 2. Comparison of the cumulative $\log(N) - \log(S)$ distribution found in each of the separate observations and in the combined image. Only sources from the inner region, contained in all four observations, have been used and incompleteness correction has not been applied. The incompleteness begins to have effect at a few $\times 10^{-15}$ $\text{erg s}^{-1} \text{cm}^{-2}$ for the combined image and at $\sim 7 - 8 \times 10^{-15}$ $\text{erg s}^{-1} \text{cm}^{-2}$ for the individual observations.

Another potential problem could be merging of sources. We have used a high value (80 per cent) of the enclosed percentage of PSF in CIAO wavdetect because it gives a good estimation of source parameters. On the other hand, such a high value in some cases leads to two sources being detected as one source. To check for this, we ran CIAO wavdetect again with smaller enclosed percentages of the PSF. We find no sources that are merged because of the high enclosed percentage of the PSF.

After the filtering, the final list of X-ray sources contains 272 objects. It is presented in Table A.1. Kraft et al. (2001) analysed the two ACIS-I observations of Cen A (Table 1) and detected 246 X-ray sources. Of these, 205 sources are located within $r < 10'$ of the center of the galaxy analysed here. 184 of these sources are in our source list, which therefore contains 90 previously undetected sources. The $\sim 1/3$ increase in the total number of detected sources is due to a factor of $\gtrsim 2 - 4$ increase in the exposure time of the main body of the galaxy (Fig. 1, Table 1).

3.1. Background and foreground sources

A fraction of the detected sources are foreground or background objects. Some (but not all) of them can be identified using either their X-ray spectra, or from observations at other wavelengths. Since this paper concerns the statistical properties of the X-ray point source population, we have adopted the following strategy. We exclude foreground sources as much as

possible, but do not attempt to remove background sources, which are by far the most significant contaminating factor. Their contribution to the surface brightness and luminosity distributions is instead taken into account in the statistical sense, based on the results of the cosmic X-ray background (CXB) source counts.

3.2. Optical identifications

We check the absolute astrometry using USNO-B1.0 (Monet et al. 2003) and GSC 2.2 (Morrison et al. 2001) catalogues. We find that for a search radius of $2.0''$ the rms deviation of the positions is $1.1''$. This is comparable to the quoted positional uncertainties of the optical catalogues as well as that of the Chandra X-ray source list, confirming reasonable astrometric accuracy of the latter. Adding a systematic shift of $0.5''$ in any direction results in larger rms deviations. The number of matches is significantly higher than the expected number of chance coincidences. For the search radius of $2.0''$ the expectation value is ~ 8 with 37 matches found for USNO-B1.0 and ~ 3 with 18 matches found for GSC 2.2.

For the actual identification of Chandra sources we used the results of the dedicated optical studies of the Cen A region by Peng et al. (2004), Minniti et al. (2003) and Woodley et al. (2005). Although the former three surveys were aimed specifically at globular cluster population of Cen A they also have identified a number of foreground stars, H_{α} emitters and sev-

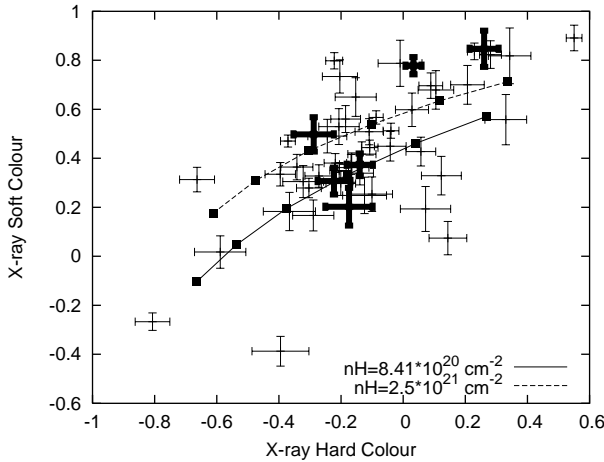


Fig. 3. The color–color diagram of the brightest, > 200 counts, sources within 5 armin from the centre of Cen A. The sources coinciding with $H\alpha$ -emitting regions are shown in bold. For reference, the two lines show the hardness ratios of power law spectra for two different values of absorption. The filled squares are at photon indices of 0.5, 1.0, 1.5, 2.0, 2.5, 3.0 from right to left. The hard and soft colours are defined as $HC = (H-M)/(H+M)$, $SC = (M-S)/(M+S)$, where S, M and H are the number of photons detected in the 0.5–1.0 keV, 1.0–2.0 keV and 2.0–8.0 keV energy range respectively.

eral AGNs. We also used results of Graham & Fasset (2002). In total we identified 6 X-ray sources as foreground stars, leaving 266 sources of presumably extragalactic origin – either intrinsic Cen A sources or background AGNs. Of these, 37 were identified with the globular clusters in Cen A. The results of this work are presented in column 8 of Table A.1.

About $\sim 2/3$ of the USNO and GSC matches were found to be globular clusters or likely globular clusters in Peng et al. (2004) and Minniti et al. (2003). The remaining 12 out of 37 sources do not appear in these papers. This is close to, albeit slightly higher than, the number of 8 random matches expected for the value of the search radius used in the analysis. Some of these sources also might be background AGNs or undetected globular clusters. Therefore we kept them all in the sample. We note that excluding them from the following analysis does not change our results in any significant way.

3.3. $H\alpha$ -sources

Eight sources within $4'$ from the centre of Cen A coincide with $H\alpha$ -emitting regions found in Minniti et al. (2003). All of them are located in the dust lanes region, have X-ray luminosities in the $10^{36} - 5 \cdot 10^{37}$ erg s^{-1} range and can potentially be associated with high-mass X-ray binaries. The optical magnitudes of the $H\alpha$ sources indicate that they may be young star clusters as well as individual X-ray binaries. In order to search for further indications of the high-mass X-ray binary (HMXB) nature of these sources we have compared their spectral properties with other sources and searched for periodic variability in their X-ray emission. As discussed in more details below, no coherent pulsations have been detected from any of the bright X-ray

sources, although the upper limits are at a rather moderate level of ~ 25 per cent pulsed fraction.

The accreting X-ray pulsars, constituting the vast majority of the neutron star HMXBs, are known to have notably harder spectra in the ~ 1 –20 keV energy range than LMXBs and often show significant intrinsic absorption. Therefore comparison of the spectral properties of the $H\alpha$ objects with other X-ray sources (which in the central part of Cen A are mostly LMXBs, Sect. 4) can help to clarify the nature of the former. However, the X-ray colour–colour diagram of the sources within $5'$ from the centre of Cen A, shown in Fig 3, does not reveal systematic difference between $H\alpha$ and other sources. Nor have we found any systematic difference from the direct spectral fits of the brightest sources. As our results were not conclusive enough, we decided to keep the $H\alpha$ sources in the sample, bearing in mind that their nature still needs to be clarified. Due to their relatively small number they do not significantly affect the following analysis of the spatial and luminosity distributions.

3.4. Globular cluster sources

37 X-ray sources coincide with known globular clusters. Interpreting this number, one should take into account that only $\sim 20 - 25$ per cent of the expected number of globular clusters in Cen A have been identified (Woodley et al. 2005). The identified sample is strongly biased, both with respect to the spatial distribution of the clusters and their luminosity distribution. Furthermore, the detection of the globular clusters is not independent of the X-ray observations, as X-ray source catalogues have been used to search for globular clusters (e.g. Minniti et al. 2003). It is therefore not possible to do rigorous comparison of the luminosity function and spatial distribution of the globular cluster X-ray sources with the sources residing outside globular clusters. Considering the sources brighter than $3 \cdot 10^{37}$ erg s^{-1} (i.e. unaffected by the incompleteness effects) there are 15 known globular cluster X-ray sources, whereas the number of sources outside globular clusters is 40. If the expected number of 22 CXB sources (see Sect. 4.3) is subtracted, we find 18 'field' LMXBs outside (or in undetected) globular clusters. Above this luminosity the XLF of globular cluster sources is similar to that of the field LMXBs. Below this luminosity the field LMXB XLF is much steeper than that of globular cluster sources. This can easily be caused by the incompleteness effects, which can not be corrected for without knowledge of the spatial distribution of the globular cluster sources (see Appendix). We also note that in the outer region there are 7 globular cluster sources, with $L_X \geq 10^{37}$ erg s^{-1} whereas we expect ~ 9 LMXBs in total (see Sect. 4.1.1).

3.5. Search for coherent pulsations

We searched for periodic variability in the light curves of the sources with more than 400 detected source counts and more luminous than $6.0 \cdot 10^{37}$ erg s^{-1} (24 sources in total). Each *CHANDRA* observation was tested separately. Events were extracted from the 4 sigma source ellipses in *wrecon* and the light curves with ≈ 3.2 sec time resolution were produced.

Table 3. Expected and observed numbers of point sources (section 4.1).

L_X erg s ⁻¹	Predicted				Obs.	
	LMXB	HMXB	CXB ⁽¹⁾	Total ⁽¹⁾	Total ⁽²⁾	
$> 10^{37}$	81	10	34 (47)	125 (138)	136	
$> 2 \cdot 10^{36}$	155	27	98 (135)	280 (317)	321	

(1) – the CXB numbers are based on the soft (hard) band counts from Moretti et al. (2003), see Sect. 4.1.3; (2) – after the incompleteness correction

The power spectra were calculated using the STARLINK² task *period*. The pulsations have been searched in the range of trial periods from $P \approx 6.4$ s, defined by the Nyquist frequency of the Chandra time series, to $P = 2000$ s. Aside from 3 sources showing variability due to the telescope dithering carrying them over the detector edge, in only one case the power exceeded the level corresponding to 99 per cent confidence. The period of 55.8 s was found for the source #135 (Table A.1) in Obs 2978 and had a significance of 99.4 per cent. This significance takes into account the number of trial periods in one power spectrum but not the number of power spectra analyzed (74). In the other 3 observations of the source the power density spectrum did not show any sign of pulsations at this period. Given the total number of power spectra investigated it is likely that this detection is a result of a statistical fluctuation. Finally, we note that even for the most luminous sources pulsed fractions of ~ 25 per cent would be needed for detection at the 99 per cent confidence level.

4. Populations of X-ray sources in the field of Centaurus A

In the central $r < 10'$ of Cen A (excluding the nucleus and the jet, Fig.1, Sect. 2) we detected 136 sources with $L_X > 10^{37}$ erg s⁻¹ and 252 (≈ 321 after the incompleteness correction) sources with $L_X > 2 \cdot 10^{36}$ erg s⁻¹ (Table A.1, 3).

4.1. Expected numbers

4.1.1. Low mass X-ray binaries

LMXBs are related to the population of old stars, and there is therefore a correlation between their number and the stellar mass of a galaxy (Gilfanov 2004). In order to estimate the expected number and luminosity distribution of LMXBs we used a *K*-band image from 2MASS Large Galaxy Atlas (Jarret et al. 2003) and integrated the flux emitted in the parts of Cen A analysed in this paper. This gives the *K*-band luminosity of $L_K = 8.6 \cdot 10^{10} L_\odot$. To convert it to the stellar mass we use the color-dependent *K*-band mass-to-light ratio from Bell & De Jong (2001). For the extinction corrected optical color of Cen A, $(B - V) \approx 0.88$, the mass-to-light ratio is $M_*/L_K \approx 0.76$. This gives the stellar mass of $5.5 \cdot 10^{10} M_\odot$, assuming that the absolute *K*-band magnitude of the sun is equal to $M_{K,\odot} = 3.39$. Using the results of Gilfanov (2004)

we predict ≈ 81 LMXBs with $L_X > 10^{37}$ erg s⁻¹, and ≈ 155 with $L_X > 2 \cdot 10^{36}$ erg s⁻¹.

4.1.2. High mass X-ray binaries

Being young objects, HMXBs are associated with star formation and, as expected for an elliptical galaxy, are by far a less significant contribution to the population of X-ray binaries than LMXBs. In terms of absolute rates, star formation in Cen A is mostly associated with the dust disk. From their analysis of IRAS data, Marston & Dickens (1988) found the total far infra-red (FIR) luminosity of the Cen A disc to be $9.7 \cdot 10^9 L_\odot$ ($L_\odot = 3.8 \cdot 10^{33}$ erg s⁻¹). From this luminosity we subtracted the emission from the central region which is mostly due to the active nucleus, $1.5 \cdot 10^9 L_\odot$, and corrected the distance from the 5 Mpc assumed in Marston & Dickens (1988) to the 3.5 Mpc adopted in this paper. This gives $L_{\text{FIR}} \approx 4.0 \cdot 10^9 L_\odot$. Assuming that the total infrared luminosity is $L_{\text{TIR}} \approx 2L_{\text{FIR}}$ and using the SFR calibration of Kennicutt (1998) we find $\text{SFR} \approx 1.4 M_\odot \text{ yr}^{-1}$. We used calibration of Grimm et al. (2003) to calculate the expected number of HMXBs (see comment in Shtykovskiy & Gilfanov 2005, regarding the normalization). From this we get the expectation of ≈ 10 HMXBs brighter than 10^{37} erg s⁻¹, and ≈ 27 sources brighter than $2 \cdot 10^{36}$ erg s⁻¹.

4.1.3. Background X-ray sources

To estimate the number of background sources we use results of the CXB $\log(N) - \log(S)$ determination by Moretti et al. (2003). Namely, we use the source counts in the soft and hard bands (their Eq. 2) and convert the fluxes to the 0.5–8.0 keV band, assuming a powerlaw spectrum with a photon index of 1.4. For the total area of our survey of 0.079 deg^2 we obtain from the source counts in the soft band ≈ 34 CXB sources above the flux corresponding to 10^{37} erg s⁻¹, and ≈ 98 above 10^{36} erg s⁻¹. From the hard band counts the predicted numbers are ≈ 47 and ≈ 135 sources. The predictions based on the soft and hard $\log(N) - \log(S)$ differ because of the well recognized fact that source counts in different energy bands and flux regimes are dominated by different types of sources. This is further discussed in Sect. 4.3.

The results of the above calculations are summarized in Table 3. For the total number of point sources, the agreement between observed and predicted is surprisingly good, given the amplitude of uncertainties involved. In the following two subsections we derive from the data, and compare with the predictions, the abundances of individual types of X-ray sources. This is done in two independent ways – based on the radial distribution of the sources (Sect. 4.2) and on their flux/luminosity distribution (Sect. 4.3).

4.2. Spatial distribution of point sources

We begin the consideration of the spatial distribution of the point sources with the azimuthally averaged radial profile (Fig.4). As it follows from the results of the previous section the

² <http://www.starlink.ac.uk>

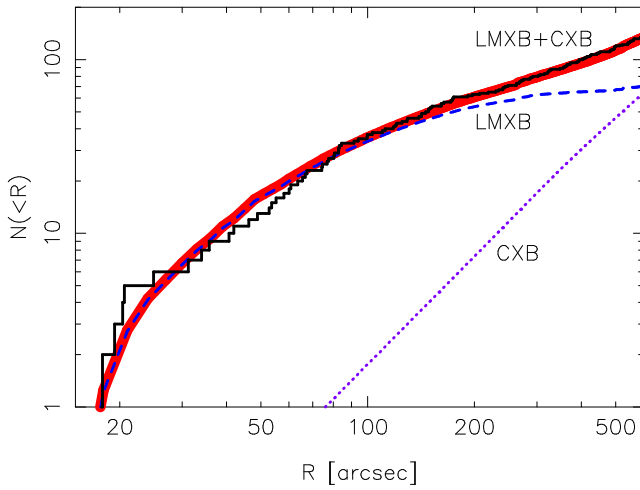


Fig. 4. The radial distribution of observed sources (solid line), compared to the best fit model (thick grey line) and the contributions of LMXBs and CXBs

two major contributors to the population of point sources in the field of Cen A are low-mass X-ray binaries ($\sim 1/2$ – $2/3$ of the sources, depending on the luminosity) and background AGNs ($\sim 1/3$ – $1/2$). Correspondingly, we model the observed distributions as a superposition of two functions, describing their respective contributions. The spatial distribution of the LMXBs has been shown (Gilfanov 2004) to follow, to the first approximation, the distribution of the stellar mass. The latter can be represented by the distribution of the K -band light and was computed using the K -band image of Cen A from the 2MASS Large Galaxy Atlas (Jarret et al. 2003). The density of the CXB sources can be assumed flat on the angular scales under consideration, therefore the CXB growth curve is proportional to the enclosed solid angle. In computing both radial profiles we took into account that some areas were excluded from the analysis (Fig.1). The only free parameter of the model is the ratio of normalizations of the LMXB and CXB distributions. The (unknown) distribution of HMXBs has not been included as it is unlikely to exceed 10% in the total number of sources (Sect. 4.1.2).

The model has been compared with the observed distribution of sources more luminous than 10^{37} erg s $^{-1}$. This value of the luminosity threshold was chosen in order to include as many sources as possible and, on the other hand, to keep incompleteness effects insignificant. The model adequately describes the data (Fig.4) as confirmed with the KS-test, which gave the probability of 96 per cent. The best fit LMXB fraction, determined from the Maximum Likelihood (M-L) fit to the unbinned radial distribution data, is 51.7 ± 5.9 per cent, corresponding to 70.3 ± 10.0 LMXBs and 65.7 ± 9.8 CXB sources. Comparing with the Table 3, the abundance of LMXBs is surprisingly close to the expectation value. The number of CXB sources, on the other hand, is higher than the expectation. This will be further discussed in Sect. 4.3.

The same LMXB+CXB model was also compared with the radially averaged azimuthal and two-dimensional distributions. The KS test of the unbinned two-dimensional distribu-

tion of the point sources (e.g. Press et al. 1992) gave the probability of 24%. The azimuthal distribution of the sources within $5'$ (to exclude the outer regions dominated by CXB) has the KS-probability of 10–20 per cent depending on the starting point.

This analysis confirms that within the statistical accuracy of the data, the spatial distribution of the LMXBs is consistent with that of the K -band light. This implies, in particular, that no additional component corresponding to HMXBs is required by the data. However, this results is not very constraining, given the rather small expected number of HMXBs, ≈ 10 .

4.2.1. Sensitivity of the spatial distribution analysis

In order to probe the sensitivity of the above analysis we performed the following test. The LMXB distribution was stretched with respect to the center of the galaxy by some scale factor, the new best fit value of the CXB to LMXB ratio was found using same method as before, and the consistency of new best fit model with the data was checked with the KS test. Then the range of values or the scale factor was found beyond which the KS probability decreased below 5 per cent indicating deteriorated quality of the approximation. The following ranges for the scale factor values were obtained: $0.4 \lesssim \eta \lesssim 1.9$ for the radial profile analysis and $0.2 \lesssim \eta \lesssim 2$ for the 2-dimensional image.

These numbers indicate a rather moderate sensitivity of the spatial distribution analysis. Sensitivity limitations of this kind are unavoidable when analysing individual galaxies. Further exposure of the inner $10'$ of the galaxy can improve the luminosity limit below which incompleteness effects have to be taken into account. Observations with the aimpoint closer to the outskirts of the galaxy could be useful too, as they could help to constrain the local CXB normalization. Finally, a very careful study of the source distribution at luminosities where incompleteness is a problem could increase the sensitivity. Another approach is to study combined source density distributions for several (many) galaxies.

4.3. Source counts and the cosmic X-ray background source density

We divided Cen A into three annuli according to the ratio of predicted numbers of LMXBs and CXB sources: $r < 2.5'$, $r = 2.5 - 5'$, $r = 5 - 10'$. The inner and outer regions are expected to be dominated by LMXBs and CXB sources respectively, while the middle one contains comparable numbers of sources of both types (e.g. Fig.4). In analysing the luminosity functions and $\log(N) - \log(S)$ distributions we used the procedure described in Appendix A to correct for incompleteness effects.

We estimate the normalization of the CXB $\log(N) - \log(S)$ distribution from the source counts in the outer region. This region is far enough from the inner parts of the Cen A to keep the number of sources related to the galaxy low, while close enough to the aimpoints of the observations to have a reasonable sensitivity. In this region the incompleteness corrected

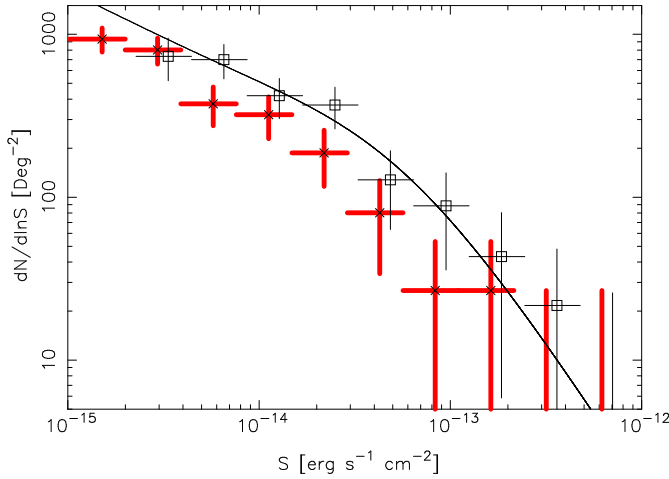


Fig. 5. The source counts in the outer region ($5' < r < 10'$). The predicted contribution of LMXBs is subtracted. The thick solid line shows the CXB $\log(N) - \log(S)$ from Moretti et al. (2003), with best fit normalization from this paper. For comparison the source counts in the CDF-N Obs-ID 1671 are shown (crosses).

number of sources with the 0.5–8 keV flux exceeding $2.7 \cdot 10^{-15}$ $\text{erg s}^{-1} \text{cm}^{-2}$ (luminosity $4.0 \cdot 10^{36} \text{ erg s}^{-1}$) is 101.3 from which 13.4 are expected to be LMXBs. The implied number of CXB sources is ≈ 88 , which we compare with the results of the radial profile analysis from the previous section and with results of dedicated CXB source counts. For this comparison we express the CXB normalization in units of the number of sources per deg^2 with 0.5–8.0 keV flux $S_X > 6.8 \cdot 10^{-15} \text{ erg s}^{-1} \text{cm}^{-2}$. The results of the CXB surveys are transformed to the 0.5–8.0 keV energy range assuming a power law spectrum with the photon index of 1.4. We used the source counts in both their soft (0.5–2.0 keV) and hard (2.0–8.0 keV) bands. The results are shown in the two columns in the upper part of Table 4. The last two lines in Table 4 present the results of the radial profile analysis and of the source counts in the $r = 5' - 10'$ ring. Note that although these two numbers are not statistically independent, they are obtained from different considerations. The radial profile analysis is based on sources with $L_X \geq 10^{37}$ erg s^{-1} in the entire $r \leq 10'$ region and relies heavily on the assumption about the spatial distribution of the LMXB component. The source counts in the outer region use all sources in the $5' \leq r \leq 10'$ with a luminosity above $10^{36} \text{ erg s}^{-1}$ and are significantly less dependent on the assumption regarding the LMXB spatial distribution.

As it has been already mentioned, there is a significant difference between the normalizations found from the hard and soft band. This is related to the fact that different types of sources give dominant contributions to the hard and soft bands. Theoretically, the two bands can be reconciled using different spectral shapes for the flux conversion, but this would introduce additional uncertainties and an investigation of this kind is beyond the scope of this paper. In addition to this, there is also a considerable spread in the CXB normalizations in the same energy band obtained in different surveys. Partly this spread is due to the cosmic variance and partly it is likely to be caused

Table 4. CXB normalization found in various surveys and in this paper.

Survey	soft band	hard band
CDF-S	332 ± 70	686 ± 71
CDF-N	437 ± 80	791 ± 73
Cappelluti et al., 2004	350 ± 28	419 ± 43
Cowie et al., 2002	–	456 ± 30
Moretti et al., 2003	422	579
Obs-ID 1671 (CDF-N)	519 ± 71	
Radial profile	832 ± 124	
$5' < r < 10'$ counts	804 ± 86	

The normalization is expressed as the number of sources per deg^2 with 0.5 – 8.0 keV flux $S_X > 6.8 \cdot 10^{-15} \text{ erg s}^{-1} \text{cm}^{-2}$. The two columns give the numbers computed from the soft and hard band counts respectively. The for CDF-fields data listed in the upper part of the table are from Rosati et al. (2002), in the lower part – from this paper.

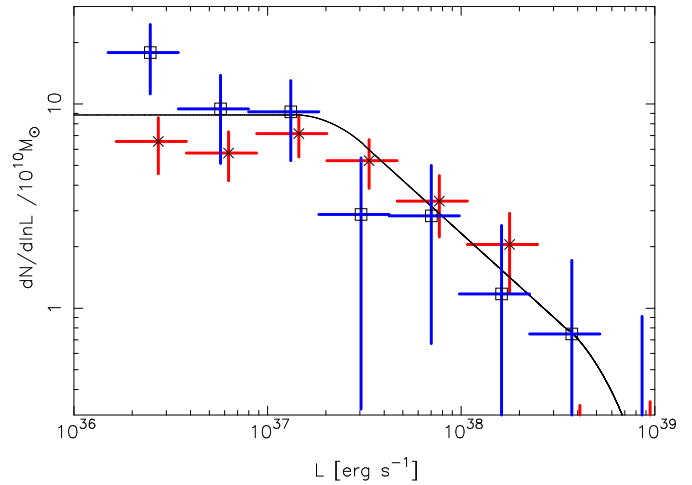


Fig. 6. The differential luminosity functions of LMXBs in the innermost (stars) and middle (squares) annuli, normalized to $10^{10} M_\odot$ of stellar mass. The CXB contribution is subtracted using the results of Sect. 4.3. The solid line shows the average LMXB XLF from Gilfanov (2004) smoothed with the boxcar filter with the logarithmically constant width equal to the bin width in the observed XLFs.

by the difference in the analysis procedures and relative calibrations of different instruments.

In order to do a direct comparison with the empty fields source counts in the 0.5 – 8.0 keV energy band, we have analysed one observation from the CDF-N (Obs-ID 1671), using the same data analysis procedure as we used for Cen A. The column density of neutral hydrogen, which was set to $1.5 \cdot 10^{20} \text{ cm}^{-2}$ (Dickey & Lockman 1990). To avoid incompleteness effects, we only used sources observed in regions with exposure above $4.4 \cdot 10^7 \text{ s cm}^2$. This limits the field to 0.058 deg^2 . Above a flux of $2.7 \cdot 10^{-15} \text{ erg s}^{-1} \text{cm}^{-2}$ (equal to the flux used to estimate the CXB normalization in the outer region of Cen A) we find 53 sources. This number can be directly compared with 88 CXB sources detected in the outer annulus in the Cen A field (accidentally, the two areas coincide). In order to facili-

tate comparison with the other CXB surveys, we transform this number to the units of Table 4, using the $\log(N) - \log(S)$ from the soft band of Moretti et al. (2003).

Even with the spread in values found from the various surveys, the CXB normalization in the Cen A field appears to be higher than the typical numbers obtained in the dedicated CXB studies, with exception of the hard band counts of the Chandra Deep Fields, according to the analysis of Rosati et al. (2002). The latter two excluded, the density of CXB sources appears to be enhanced by a factor of $\sim 1.4 - 2$. Although this is larger than the rms variation between different fields typically quoted in the literature, $\sim 20 - 25$ per cent, the observed number is not exceptionally high and still lies within the spread of the CXB density values (e.g. Cappelluti et al. 2004).

4.4. LMXB X-ray luminosity function

The luminosity function of LMXBs determined from the two inner regions is shown in Fig.6. In subtracting the contribution of CXB sources we used the $\log(N) - \log(S)$ distribution from Moretti et al. (2003) with the normalization determined in the Sect. 4.3. Note that while the CXB contribution is unimportant in the innermost region $r \leq 2'5$, it accounts for about half of the sources in the middle region $2'5 \leq r \leq 5'$. As obvious from Fig.6, both distributions are consistent with each other and with the average LMXB XLF in the local galaxies determined by Gilfanov (2004), with possible exception of the the lowest luminosity bin of the middle region, which deviates by $\sim 1.5\sigma$.

To further constrain the parameters of LMXB XLF in Cen A we fit the luminosity distribution in the inner region with a power law with two breaks, identical to the one used in Gilfanov (2004). Since there are no sources luminous enough to constrain the upper break and the slope beyond that, we have fixed them at the average values: $L_{b2} = 5.0 \cdot 10^{38}$ erg s $^{-1}$, $\alpha_3 = 4.8$. The best fit values of other parameters are: the low luminosity slope $\alpha_1 = 1.02^{+0.12}_{-0.13}$, a break at $L_{b1} = 5.0^{+1.0}_{-0.7} \cdot 10^{37}$ erg s $^{-1}$ and a slope after the break $\alpha_2 = 2.6 \pm 0.4$. The slopes refer to the differential distribution, the parameter errors are 1σ statistical errors only. These parameters are insensitive to whether the CXB component is accounted for or not.

A large uniformly analysed sample of the XLF of LMXBs in elliptical galaxies was presented by Kim & Fabbiano (2004). They find an average differential slope of 1.8 ± 0.2 in the luminosity range $L_X = \text{a few} \times 10^{37}$ to 5×10^{38} erg s $^{-1}$. This is consistent with our results from the inner region. A KS-test gives 73 per cent probability that the observed luminosity distribution above $L_X = 1.0 \cdot 10^{37}$ erg s $^{-1}$ could be produced by their LMXB XLF. On the other hand it is clear that at the faint end of the XLF the extrapolation of their results is inconsistent with our observations. For sources more luminous than $L_X = 5.0 \cdot 10^{36}$ erg s $^{-1}$, a similar KS-test gives 3.4 per cent, and for lower luminosities the probability decreases further.

The LMXB XLF based on the combined data of $r \leq 5'$ is plotted in Fig.7 along with luminosity distributions of LMXBs in the Milky Way and M31. This plot further illustrates qualitative and quantitative similarity of the LMXB luminosity distri-

butions in Cen A and bulges of spiral galaxies. This is the first study to extend the LMXB XLF in elliptical galaxies below $\sim \text{few} \times 10^{37}$ erg s $^{-1}$. Spiral and elliptical galaxies have different evolutionary histories and it could differ in the properties of their LMXB populations. As demonstrated here, the luminosity functions nevertheless seem very similar, except for the break luminosity which could be somewhat higher in Cen A than in the Milky Way and M31. Whether this reflects a systematic difference between LMXBs in galaxies of different type is yet to be investigated.

4.5. X/M_* ratios

In the inner (middle) region there are 53 (27) sources with $L_X > 10^{37}$ erg s $^{-1}$, with an integrated luminosity of $L_X = 2.3 \cdot 10^{39}$ ($1.3 \cdot 10^{39}$) erg s $^{-1}$. We expect the CXB contribution to be $N_{\text{CXB}} = 3.8$ (13.4), corresponding to a luminosity of $1.9 \cdot 10^{38}$ ($6.7 \cdot 10^{38}$) erg s $^{-1}$. From the K -band light we estimate that the stellar mass is $3.6 \cdot 10^{10}$ ($1.3 \cdot 10^{10}$) M_\odot , and this gives us the ratios $N_X/M_* = 13.7 \pm 1.9$ (10.5 ± 2.0) sources per $10^{10} M_\odot$ and $L_X/M_* = 6.4$ (4.8) $\times 10^{38}$ erg s $^{-1}$ per $10^{10} M_\odot$. The values for the two regions are consistent. They are also in a good agreement with the values for different nearby galaxies listed in Table 2 of Gilfanov (2004) as well as with the average values of $\langle N_X/M_* \rangle = 14.3$ and $\langle L_X/M_* \rangle = 8.0 \cdot 10^{38}$ erg/s per $10^{10} M_\odot$.

The X/M_* ratios obtained in this paper are by a factor of 2 lower than the values for Cen A in Gilfanov (2004). We note that he reported problems in approximating the multi-aperture K -band photometry data for Cen A galaxy. Indeed, we recomputed the K -band luminosity for the same region using the 2MASS K -band image and obtained ≈ 2 times larger number. This explains the lower values of N_X/M_* and L_X/M_* found in this paper. As these numbers are derived from the real K -band images rather than from extrapolation of the multi-aperture K -band photometry, they better represent the true values of the X/M_* ratios.

5. Summary and conclusions

We have used archival data of *CHANDRA* observations to study statistical properties of the point source population of Cen A. Our primary goal was to investigate the faint end of the LMXBs luminosity distribution in an elliptical galaxy and to compare it with LMXB XLF in bulges of spiral galaxies. To achieve this we assembled as deep a survey of the central part of the galaxy as permitted by the available data and implemented an adequate correction for the incompleteness effects.

Using a combined image of four ACIS observations (Table 1, Fig.1) with the total exposure time of 170 ks we have detected 272 point-like sources within $10'$ from the nucleus of Cen A. The luminosity of the weakest detected source is $\approx 9 \cdot 10^{35}$ erg s $^{-1}$ (assuming the distance of 3.5 Mpc), while the source sample starts to be affected by the incompleteness effects below $\sim 10^{37}$ erg s $^{-1}$ (Fig.A.1). After correction for incompleteness, the total number of sources with $L_X \geq 2 \cdot 10^{36}$ erg s $^{-1}$ is ≈ 321 . This number is in a good agreement with the prediction based on the stellar mass, the star formation rate in

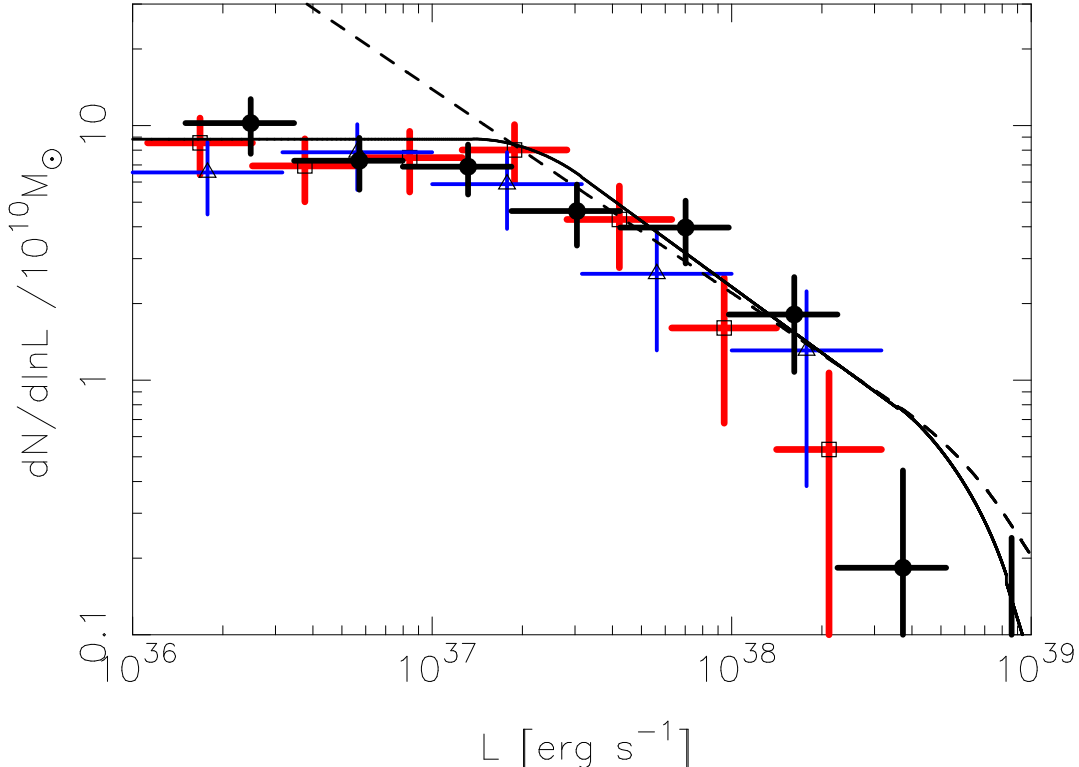


Fig. 7. The luminosity function of LMXBs in the inner $r \leq 5'$ of Cen A (the CXB contribution subtracted) in comparison with LMXB XLFs in the Milky Way (triangles) and M31 (squares) (from Gilfanov 2004). The latter two are multiplied by constant factors of 1.7 and 0.6 respectively. The solid line shows the average LMXB XLF in the nearby galaxies as determined by Gilfanov (2004), the same as in Fig.6. The dashed line shows the average LMXB XLF from Kim & Fabbiano (2004) and its extrapolation towards low luminosities. Its normalization was chosen to approximately match our observations.

Cen A and the density of CXB sources (Table 3). About half of the detected sources are expected to be X-ray binaries in Cen A, mostly LMXBs; the vast majority of the remaining sources are background galaxies constituting the resolved part of the CXB.

The spatial distribution of the detected sources can be well described by a sum of two components. Of these, one has the density proportional to the K -band light (Fig.4) and the other is uniform across the Cen A field. We interpret that the former represents low-mass X-ray binaries in Cen A while the latter accounts for the resolved part of the CXB. The normalization of the LMXB component agrees well with the average value derived for the local galaxies by Gilfanov (2004). The normalization of the uniform component and source counts in the exteriors of the galaxy appear to indicate an overabundance of the CXB sources in the direction of Cen A by a factor of ~ 1.5 or, possibly, more (Table 4, Fig.5).

After applying the incompleteness correction and subtracting the contribution of CXB sources we were able to recover the the LMXB luminosity function in the inner $r \leq 5'$ down to $L_X \sim 2 \cdot 10^{36}$ erg s $^{-1}$ (Fig.6,7). This is by a factor of $\sim 5 - 10$ better than achieved previously for any elliptical galaxy (Kraft et al. 2001; Kim & Fabbiano 2004). The shape of the luminosity distribution is consistent with the average LMXB XLF in nearby galaxies derived by Gilfanov (2004) and for the bright end by Kim & Fabbiano (2004). In partic-

ular, we demonstrate that the LMXB XLF in Cen A flattens at the faint end and is inconsistent with extrapolation of the steep power law with differential slope of $\approx 1.8 - 1.9$ observed above $\log(L_X) \sim 37.5 - 38$ in the previous studies of elliptical galaxies. Rather, the LMXB XLF in Cen A has a break at $L_X \approx (5 \pm 1) \cdot 10^{37}$ erg s $^{-1}$ below which it follows the $dN/dL \propto L^{-1 \pm 0.1}$ law, similar to the behaviour found in the bulges of spiral galaxies.

Acknowledgements. This reaserch has made use of *CHANDRA* archival data provided by the *CHANDRA* X-ray Center and data from the 2MASS Large Galaxy Atlas provided by NASA/IPAC infrared science archive.

References

- Bell, E., & De Jong, R. 2001, ApJ, 550, 212
- Bildsten, L., & Deloye, C.J. 2004, ApJ, 607, L119
- Cappelluti, N., Cappi, M., Dadina, M., et al., 2004, astroph, 0409434
- Colbert, E.J.M., Heckman, T.M., Ptak, A.F., Strickland, D.K., & Weaver, K.A. 2004, ApJ, 602, 231
- Cowie, L.L., Garmire, G.P., Bautz, M.W., et al. 2002, ApJ, 566, L5
- Dickey, J.M., & Lockman, F.J. 1990, ARA&A, 28, 215
- Evans, D.A., Kraft, R.P., Worrall, D.M., et al. 2004, ApJ, 612, 786

Freeman, P.E., Kashyap, V., Rosner, R., & Lamb, D.Q. 2002, *ApJ SS* 138, 185

Gilfanov, M., 2004, *MNRAS* 349, 146

Graham, J.A., & Fasset, C.I. 2003, *ApJ*, 575, 712

Grimm, H.-J., Gilfanov, M.R., & Sunyaev, R.A. 2003, *MNRAS*, 339, 793

Hardcastle, M.J., Worrall, D.M., Kraft, R.P., et al. 2003, *ApJ* 593, 169

Israel, F.P. 1998, *A&A Rev.*, 8, 237

Jarret, T.H., Chester, T., Cutri, R., Schneider, S., & Huchra, J.P. 2003, *AJ* 125, 525

Karovska, M., Fabbiano, G., Nicastro, F., et al. 2002, *ApJ*, 577, 114

Kennicutt, R.C. 1998, *ARA&A*, 36, 189

Kim, D.-W., & Fabbiano, G. 2004, *ApJ*, 611, 846

Kraft, R.P., Kregenow, J.M., Forman, W.R., Jones, C., & Murray, S.S. 2001, *ApJ*, 560, 675

Kraft, R.P., Forman, W.R., Jones, C., et al. 2002, *ApJ*, 569, 54

Kraft, R.P., Vázquez, S.E., Forman, W.R., et al. 2003, *ApJ*, 592, 129

Marston, A.P., & Dickens, R.J. 1988, *A&A*, 193, 27

Minniti, D., Rejkuba, M., Funes, J.G., & Akiyama, S. 2003, *ApJ*, 600, 716

Monet, D.G., Levine, S.E., Canzian, B., et al. 2003, *AJ*, 125, 984

Moretti, A., Campana, S., Lazzati, D., & Tagliaferri, G. 2003, *ApJ*, 588, 696

Morrison, J.E., Röser, S., McLean, B., Bucciarelli, B., Lasker, B. 2001, *AJ*, 121, 1752

Peng, E.W., Ford, H.C., & Freeman, K.C. 2003, *ApJ SS*, 150, 367

Postnov, K.A., & Kuranov, A.G. 2004, *Astroph*, 0411407

Press, W.H., Teukolsky, S.A., Vetterling, W.T., & Flannery, B.P. 1992, *Numerical recipes in C. The art of scientific computing*, University Press, Cambridge

Roeser, S., Bastian, U., & Wiese, K. 1991, *A&A SS*, 88, 277

Rosati, P., Tozzi, P., Giacconi, R., et al. 2002, *ApJ*, 556, 667

Schiminovich, D., van Gorkom, J.H., van der Hulst, J.M., & Kasow, S. 1994, *ApJ*, 423, L101

Shtykovskiy, P., & Gilfanov, M. 2005, *A&A*, 431, 597

Woodley, K.A., Harris, W.E., & Harris, G.L.H. 2005, *Astroph*, 0503158

Appendix A: Correction for incompleteness

The variations of the diffuse background level and deterioration of the point spread function at large off-axis angles lead to variations of the point-source sensitivity across the Chandra images. In the case where several observations with different pointing directions are combined together, this effect is further amplified by the non uniform exposure of the combined image. As a result, the completeness of the source sample at the faint end is compromised. A trivial solution to this problem is to define a conservative sensitivity limit, which is high enough to be achieved everywhere across the image. Although simple in implementation, this method has a disadvantage that a noticeable fraction of the source has to be thrown away. Nevertheless,

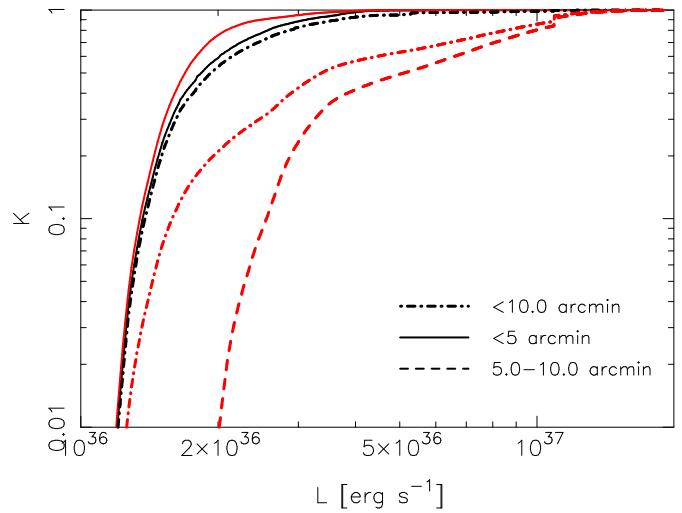


Fig. A.1. The sample incompleteness as a function of the luminosity for the inner ($< 5'$), outer (5–10') and full region. The black lines are calculated using the source density proportional to the K -band light distribution. The grey lines are calculated assuming a uniform source density.

it has been used, with few exceptions (e.g. Kim & Fabbiano 2004; Shtykovskiy & Gilfanov 2005), in the majority of the earlier studies of the point source populations in galaxies. A more effective approach to the problem is to define the correction function to the flux/luminosity distribution, which accounts for the sensitivity variations across the image. For a uniform distribution of sources this correction function simply accounts for the dependence of the survey area upon the energy flux or count rate. This is the case, for example, in the CXB studies. In a more complex case of a non-uniform distribution of point sources, the observed and real flux distributions are related via:

$$\left(\frac{dN}{dS} \right)_{\text{obs}} = \int_{S_0 \leq S} \frac{dN}{dS} \Sigma(x, y) dx dy \quad (\text{A.1})$$

where $\Sigma(x, y)$ is the surface density distribution of point sources, and for given flux S the integration is performed over the part of the image where the local sensitivity $S_0(x, y)$ satisfies the condition $S_0(x, y) \leq S$. If the flux distribution does not depend on the position, it can be easily recovered from the above equation. Importantly, knowledge of the spatial distribution of sources is required in order to recover the flux distribution and vice versa. If both flux and density distributions are unknown, the sample incompleteness can not be properly accounted for. The problem is further complicated by the contribution of the CXB sources, having a different spatial and flux distributions:

$$\begin{aligned} \left(\frac{dN}{dS} \right)_{\text{obs}} = & \int_{S_0 \leq S} \left(\frac{dN}{dS} \right)_{\text{LMXB}} \Sigma_{\text{xb}}(x, y) dx dy \\ & + \int_{S_0 \leq S} \left(\frac{dN}{dS} \right)_{\text{CXB}} \Sigma_{\text{cxb}}(x, y) dx dy \end{aligned} \quad (\text{A.2})$$

For the practical implementation of the correction procedure, knowledge of the source detection algorithm is of course

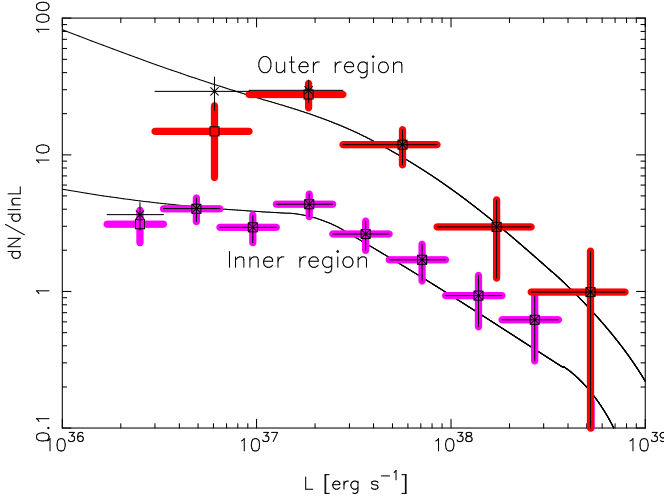


Fig. A.2. Simulated luminosity functions for the inner, $r \leq 5'$, and outer, $r \geq 5'$, regions. The input distributions (solid lines) are compared with the results obtained from the analysis of the images, done in the same way as the analysis of the real data. Both data corrected (asterisks) for incompleteness and uncorrected (squares) are shown. The normalization of the inner region has been divided by 10 for clarity.

required. The `wavdetect` task (Freeman et al. 2002) correlates the image with a Mexican Hat function and registers sources with the correlation value exceeding a threshold value. The latter is estimated numerically based on the user-specified threshold significance. For each of the used detection scales we computed the threshold sensitivity on a grid of the positions on the image (16 azimuthal angles, 40 radii from the centre of Cen A). At each image position the PSF was obtained from the CALDB PSF library for each of the four individual observations and then combined with the exposure times as weights. The local background levels were found from the normalized background maps created by `wavdetect`. The sensitivity for any given position on the image was found from interpolation of the grid values. The sample incompleteness is described by the incompleteness function:

$$K(L) = \sum_{L_0(i,j) \leq L} \Sigma(i, j) \quad (\text{A.3})$$

where i, j are the pixel coordinates and $L_0(i, j)$ is the position-dependent sensitivity. Depending on the desired normalization of the $K(L)$, the the density distribution $\Sigma(i, j)$ can be normalized to unity or, for example, be given in the units of M_\odot per pixel of the image.

If the CXB contribution can be neglected (eq.A.1), the corrected luminosity distribution can be obtained giving the weight $1/K(L)$ to a source of luminosity L . For the ML fits the model should be multiplied by the $K(L)$.

For the general case of eq.A.2, the incompleteness function $K(L)$ should be calculated for the CXB and LMXB components separately. For the LMXBs density distribution we used the K -band image, the CXB distribution was assumed to be uniform. The corresponding incompleteness functions are shown in Fig.

A.1. They demonstrate clearly importance of the spatial distribution of sources.

The results of one of our simulations are shown in Fig.A.2. In these simulations the background map from the `wavdetect` and the K -band image were azimuthally averaged. The flux/luminosity distributions for the CXB sources and LMXBs were assumed in the form described in Sects. 4.3 and 4.4. In the simulations, the sources were randomly drawn from the assumed spatial and luminosity distributions and projected to the image using the PSF data from CALDB. The image of expectation values, containing the diffuse component and the point source contribution was then randomized assuming Poission statistics. The final image was analysed using the same chain of tasks as applied to the real images. The simulated and obtained luminosity distributions are shown in Fig.A.2.

The Figs.A.1 and A.2 demonstrate that given the pattern of Chandra observations of Cen A, incompleteness effects are not of primary concern in the inner $r \lesssim 5'$ region at the luminosities above $\sim (2 - 3) \cdot 10^{36}$ erg/s. They should be taken into account, however, for the source counts in the entire image and in the outer ring.

Table A.1. The list of point like X-ray sources within $r < 10'$ from the center of Cen A.

ID (1)	Dist (2)	R.A. (3)	Dec. (4)	Total Cts (5)	Source Cts (6)	Luminosity (7)	Type (8)	ID reference (9)
1	17.5	13 25 27.0	-43 00 52.8	499	266.8	$2.36 \cdot 10^{37}$		
2	18.1	13 25 29.2	-43 01 14.6	219	78.8	$7.17 \cdot 10^{36}$	H_α	mrfa-45
3	19.1	13 25 26.5	-43 00 54.6	1905	1480.7	$1.28 \cdot 10^{38}$		
4	19.7	13 25 26.8	-43 01 26.1	523	267.1	$2.29 \cdot 10^{37}$		
5	19.8	13 25 27.5	-43 01 28.5	991	705.3	$5.99 \cdot 10^{37}$	GC	mrfa-053
6	20.2	13 25 29.5	-43 01 08.3	498	297.4	$2.52 \cdot 10^{37}$	GC	mrfa-044
7	23.3	13 25 26.6	-43 01 29.4	118	51.6	$5.25 \cdot 10^{36}$		
8	23.8	13 25 25.8	-43 00 56.1	1862	1578.1	$1.35 \cdot 10^{38}$	GC	mrfa-017
9	26.1	13 25 25.3	-43 01 14.3	105	61.7	$6.03 \cdot 10^{36}$		
10	26.4	13 25 29.7	-43 01 22.5	68	31.3	$3.09 \cdot 10^{36}$		
11	27.3	13 25 25.6	-43 01 24.2	259	110.3	$9.66 \cdot 10^{36}$		
12	30.6	13 25 28.5	-43 01 37.9	96	42.9	$4.01 \cdot 10^{36}$		
13	32.3	13 25 25.2	-43 01 27.1	741	565.7	$4.90 \cdot 10^{37}$	GC	mrfa-057
14	34.9	13 25 24.8	-43 01 25.0	263	181.6	$1.66 \cdot 10^{37}$		
15	35.8	13 25 24.4	-43 01 10.4	199	121.7	$1.09 \cdot 10^{37}$		
16	38.7	13 25 27.0	-43 00 30.6	172	128.5	$1.15 \cdot 10^{37}$		
17	40.5	13 25 30.9	-43 01 28.4	67	37.4	$3.54 \cdot 10^{36}$		
18	41.5	13 25 23.9	-43 00 59.0	312	227.5	$2.00 \cdot 10^{37}$		
19	43.9	13 25 31.5	-43 00 57.2	38	21.6	$2.05 \cdot 10^{36}$		
20	45.2	13 25 23.9	-43 01 27.2	61	31.1	$3.24 \cdot 10^{36}$		
21	47.6	13 25 24.4	-43 01 41.2	252	168.2	$1.51 \cdot 10^{37}$	H_α	mrfa-60
22	50.9	13 25 27.1	-43 01 59.4	825	675.6	$5.76 \cdot 10^{37}$	H_α	mrfa-54
23	52.9	13 25 27.3	-43 00 16.0	35	21.2	$2.23 \cdot 10^{36}$		
24	53.0	13 25 24.2	-43 01 45.7	84	49.3	$4.74 \cdot 10^{36}$		
25	53.1	13 25 23.4	-43 00 43.6	79	48.2	$4.61 \cdot 10^{36}$		
26	53.9	13 25 23.5	-43 01 38.7	714	589.2	$5.15 \cdot 10^{37}$		
27	54.2	13 25 22.9	-43 01 25.1	1947	1780	$1.53 \cdot 10^{38}$		
28	56.1	13 25 23.1	-43 01 34.9	226	157.3	$1.46 \cdot 10^{37}$		
29	58.9	13 25 32.5	-43 01 34.3	869	768.3	$6.41 \cdot 10^{37}$		
30	59.1	13 25 22.4	-43 01 22.3	63	33.8	$3.37 \cdot 10^{36}$		
31	59.9	13 25 33.1	-43 01 08.1	264	213.4	$1.80 \cdot 10^{37}$		
32	61.9	13 25 23.1	-43 01 45.8	406	312.7	$2.77 \cdot 10^{37}$		
33	64.4	13 25 26.9	-43 00 04.9	239	18.5	$4.84 \cdot 10^{36}$		
34	65.0	13 25 22.1	-43 01 32.4	85	59.1	$6.00 \cdot 10^{36}$		
35	65.0	13 25 33.4	-43 00 53.1	507	427.8	$3.64 \cdot 10^{37}$	H_α	mrfa-06
36	65.5	13 25 25.6	-43 02 10.5	63	46	$4.54 \cdot 10^{36}$	GC	mrfa-055
37	65.5	13 25 27.5	-43 02 14.3	1609	1496.2	$1.27 \cdot 10^{38}$		
38	68.2	13 25 31.4	-43 02 03.3	256	18.8	$1.74 \cdot 10^{37}$		
39	69.4	13 25 27.7	-43 02 18.2	288	227.8	$1.98 \cdot 10^{37}$	FS	mrfa-51
40	72.1	13 25 21.4	-43 00 46.0	51	36.9	$3.72 \cdot 10^{36}$		
41	72.9	13 25 22.9	-43 00 17.6	363	331.7	$3.02 \cdot 10^{37}$		
42	73.0	13 25 23.7	-43 00 09.7	1835	1730	$1.50 \cdot 10^{38}$	H_α	mrfa-21
43	73.2	13 25 24.8	-43 00 02.6	116	85.4	$7.40 \cdot 10^{36}$		
44	78.5	13 25 24.2	-42 59 59.7	573	521.5	$4.55 \cdot 10^{37}$	H_α	mrfa-19
45	78.8	13 25 25.3	-43 02 23.4	213	180.1	$1.63 \cdot 10^{37}$		
46	78.8	13 25 21.7	-43 01 54.2	191	137.5	$1.22 \cdot 10^{37}$		
47	78.9	13 25 31.6	-43 00 03.3	1023	962.6	$8.08 \cdot 10^{37}$	GC	pff-gc-210
48	81.2	13 25 28.8	-42 59 48.6	1107	1034.7	$8.67 \cdot 10^{37}$		
49	83.9	13 25 21.2	-43 01 55.0	212	189	$1.78 \cdot 10^{37}$		
50	84.4	13 25 23.6	-43 02 20.8	465	421	$3.73 \cdot 10^{37}$		
51	85.5	13 25 21.3	-43 01 58.9	223	174.4	$1.54 \cdot 10^{37}$		
52	93.0	13 25 21.6	-43 02 13.8	146	124.7	$1.15 \cdot 10^{37}$		
53	94.3	13 25 20.8	-43 00 10.8	27	20.3	$2.11 \cdot 10^{36}$		
54	95.8	13 25 32.0	-43 02 31.5	535	490.7	$4.17 \cdot 10^{37}$	H_α	mrfa-40
55	97.4	13 25 25.8	-42 59 33.4	33	17.4	$1.61 \cdot 10^{36}$		
56	98.1	13 25 30.3	-42 59 35.2	136	89.8	$7.58 \cdot 10^{36}$	GC	pff-gc-209
57	98.7	13 25 19.0	-43 01 37.0	67	48.6	$4.81 \cdot 10^{36}$		
58	98.9	13 25 29.0	-42 59 31.1	95	59.8	$5.10 \cdot 10^{36}$		

Table A.1. continued.

ID (1)	Dist (2)	R.A. (3)	Dec. (4)	Total Cts (5)	Source Cts (6)	Luminosity (7)	Type (8)	ID reference (9)
59	99.5	13 25 36.6	-43 00 57.6	303	233.9	$1.94 \cdot 10^{37}$		
60	99.8	13 25 18.5	-43 01 16.4	578	523.1	$4.58 \cdot 10^{37}$	GC	mrfa-074
61	100.4	13 25 19.9	-43 02 03.4	38	25	$2.69 \cdot 10^{36}$		
62	102.7	13 25 18.7	-43 01 41.2	96	72.3	$7.04 \cdot 10^{36}$		
63	104.6	13 25 19.2	-43 01 58.4	61	45.1	$5.07 \cdot 10^{36}$		
64	105.0	13 25 28.2	-43 02 53.6	368	340.1	$2.98 \cdot 10^{37}$		
65	110.2	13 25 37.4	-43 01 31.8	109	81.5	$6.81 \cdot 10^{36}$	GC	mrfa-033
66	112.0	13 25 26.8	-43 03 00.4	188	159.4	$1.40 \cdot 10^{37}$		
67	113.2	13 25 18.7	-43 02 05.8	41	27.3	$2.88 \cdot 10^{36}$		
68	113.7	13 25 22.2	-43 02 45.8	126	116.9	$1.09 \cdot 10^{37}$	GC	pff-gc-121
69	115.5	13 25 20.7	-42 59 42.1	22	12.7	$1.30 \cdot 10^{36}$		
70	118.7	13 25 30.5	-42 59 14.3	496	435.8	$3.68 \cdot 10^{37}$		
71	119.4	13 25 35.2	-43 02 34.1	150	120.8	$1.03 \cdot 10^{37}$		
72	120.4	13 25 17.9	-43 02 04.4	209	181.6	$2.10 \cdot 10^{37}$		
73	123.1	13 25 31.9	-43 03 02.5	56	38.2	$3.34 \cdot 10^{36}$		
74	125.0	13 25 27.9	-42 59 03.9	43	26.5	$2.35 \cdot 10^{36}$		
75	126.9	13 25 28.4	-43 03 15.4	251	211.5	$1.81 \cdot 10^{37}$		
76	127.6	13 25 35.5	-42 59 35.4	609	549	$5.27 \cdot 10^{37}$	GC	pff-gc-214
77	130.4	13 25 38.3	-43 02 05.8	2221	2158.8	$1.78 \cdot 10^{38}$		
78	130.6	13 25 39.5	-43 00 58.9	39	22	$1.99 \cdot 10^{36}$		
79	131.1	13 25 17.1	-43 00 07.5	46	33.9	$3.15 \cdot 10^{36}$		
80	131.5	13 25 33.4	-42 59 13.6	101	78	$7.40 \cdot 10^{36}$		
81	139.6	13 25 15.7	-43 01 58.2	58	44.7	$7.11 \cdot 10^{36}$		
82	141.2	13 25 33.7	-43 03 13.3	188	159.3	$1.36 \cdot 10^{37}$		
83	141.6	13 25 14.8	-43 00 48.7	42	21.3	$1.94 \cdot 10^{36}$		
84	142.1	13 25 40.6	-43 01 15.2	638	587	$5.02 \cdot 10^{37}$		
85	142.3	13 25 38.3	-43 02 30.5	15	9.4	$9.11 \cdot 10^{35}$		
86	143.9	13 25 23.6	-43 03 25.9	256	221.8	$2.38 \cdot 10^{37}$		
87	146.4	13 25 34.0	-42 58 59.9	558	514.4	$4.59 \cdot 10^{37}$	GC	pff-gc-159
88	147.1	13 25 20.1	-43 03 10.4	367	317.4	$3.95 \cdot 10^{37}$	GC	mrfa-071
89	147.9	13 25 16.9	-42 59 38.9	19	11.9	$1.18 \cdot 10^{36}$		
90	148.1	13 25 32.5	-42 58 50.5	206	180.8	$1.80 \cdot 10^{37}$	GC	pff-gc-178
91	148.2	13 25 22.4	-42 58 52.2	41	25.8	$2.34 \cdot 10^{36}$		
92	148.6	13 25 41.1	-43 01 26.8	607	574.2	$4.95 \cdot 10^{37}$		
93	149.6	13 25 14.0	-43 01 21.6	63	43.4	$6.44 \cdot 10^{36}$		
94	150.0	13 25 41.0	-43 00 37.7	49	25.6	$2.21 \cdot 10^{36}$		
95	152.7	13 25 16.8	-42 59 32.4	34	24.3	$2.29 \cdot 10^{36}$		
96	153.5	13 25 19.9	-43 03 17.2	2263	2028.1	$2.10 \cdot 10^{38}$		
97	155.2	13 25 24.9	-43 03 41.2	33	22.8	$2.46 \cdot 10^{36}$		
98	159.2	13 25 27.3	-42 58 29.7	68	48.3	$4.29 \cdot 10^{36}$		
99	161.0	13 25 42.0	-43 01 42.3	32	21.7	$1.98 \cdot 10^{36}$		
100	161.4	13 25 12.9	-43 01 14.7	589	527.1	$7.40 \cdot 10^{37}$	GC	mrfa-082
101	162.2	13 25 20.6	-42 58 46.0	712	676.3	$6.04 \cdot 10^{37}$		
102	162.5	13 25 16.4	-43 02 55.4	290	262.1	$3.19 \cdot 10^{37}$		
103	162.5	13 25 38.6	-42 59 20.0	99	70.5	$6.21 \cdot 10^{36}$	GC	pff-gc-164
104	167.4	13 25 12.5	-43 00 49.4	56	39.5	$5.09 \cdot 10^{36}$		
105	172.7	13 25 12.0	-43 00 44.6	343	302.3	$3.73 \cdot 10^{37}$		
106	173.2	13 25 40.1	-43 02 55.5	45	27.1	$2.34 \cdot 10^{36}$		
107	173.7	13 25 28.0	-43 04 02.5	194	167.4	$1.47 \cdot 10^{37}$	GC	mrfa-050
108	174.4	13 25 40.5	-43 02 51.8	38	26.7	$2.37 \cdot 10^{36}$	H _α	mrfa-30
109	175.0	13 25 40.8	-43 02 47.1	267	234.5	$1.97 \cdot 10^{37}$		
110	175.8	13 25 14.1	-43 02 43.2	141	118.9	$1.29 \cdot 10^{37}$	GC	mrfa-080
111	176.5	13 25 35.8	-43 03 40.9	44	33.7	$3.06 \cdot 10^{36}$		
112	180.6	13 25 12.0	-43 00 11.0	473	441.9	$3.99 \cdot 10^{37}$	FS	mrfa-85
113	180.6	13 25 29.4	-42 58 09.3	28	18	$1.96 \cdot 10^{36}$	GC	pff-gc-155
114	180.8	13 25 33.9	-42 58 21.6	78	61.6	$5.72 \cdot 10^{36}$		
115	182.7	13 25 11.1	-43 01 32.3	25	17.8	$2.54 \cdot 10^{36}$		
116	186.6	13 25 42.8	-42 59 44.0	28	17.3	$1.60 \cdot 10^{36}$		
117	187.9	13 25 28.3	-43 04 16.6	113	95.9	$8.55 \cdot 10^{36}$		

Table A.1. continued.

ID (1)	Dist (2)	R.A. (3)	Dec. (4)	Total Cts (5)	Source Cts (6)	Luminosity (7)	Type (8)	ID reference (9)
118	192.1	13 25 11.6	-43 02 26.6	184	161.9	$1.74 \cdot 10^{37}$		
119	193.9	13 25 14.5	-42 58 58.7	22	13.7	$1.37 \cdot 10^{36}$		
120	194.4	13 25 17.8	-43 03 50.6	43	29.9	$3.45 \cdot 10^{36}$		
121	197.9	13 25 45.7	-43 01 15.9	79	43.1	$3.62 \cdot 10^{36}$	GAL	whh-317
122	199.1	13 25 24.9	-43 04 25.7	151	132.9	$1.58 \cdot 10^{37}$		
123	201.8	13 25 12.2	-42 59 18.8	34	25.3	$2.57 \cdot 10^{36}$		
124	201.8	13 25 29.3	-42 57 47.8	48	23.8	$2.18 \cdot 10^{36}$	GC	whh-22
125	204.1	13 25 14.8	-42 58 40.8	33	23.2	$2.23 \cdot 10^{36}$		
126	206.0	13 25 42.1	-43 03 20.0	52	30.5	$2.59 \cdot 10^{36}$	GC	mrfa-026
127	208.6	13 25 38.2	-42 58 15.8	131	107	$9.14 \cdot 10^{36}$	GC	mrfa-003
128	208.8	13 25 32.9	-43 04 29.4	173	146.6	$1.30 \cdot 10^{37}$		
129	209.2	13 25 46.5	-43 00 36.7	54	31.1	$2.82 \cdot 10^{36}$		
130	211.5	13 25 19.1	-42 57 59.3	55	42.9	$4.28 \cdot 10^{36}$		
131	216.1	13 25 24.4	-42 57 35.6	280	7.1	$2.08 \cdot 10^{36}$		
132	216.5	13 25 13.2	-42 58 41.2	23	17.2	$1.93 \cdot 10^{36}$		
133	217.3	13 25 07.8	-43 00 59.8	24	15.9	$2.06 \cdot 10^{36}$		
134	218.7	13 25 32.3	-43 04 41.4	49	34.3	$3.27 \cdot 10^{36}$		
135	219.1	13 25 07.7	-43 01 15.5	2028	1873	$1.90 \cdot 10^{38}$	GC	whh-8
136	222.1	13 25 16.0	-43 04 11.1	31	17.2	$2.14 \cdot 10^{36}$		
137	223.0	13 25 47.7	-43 00 30.7	89	45	$4.18 \cdot 10^{36}$		
138	228.5	13 25 43.2	-42 58 37.6	152	120.9	$1.04 \cdot 10^{37}$	GC	pff-gc-062
139	229.0	13 25 09.4	-42 59 17.6	78	45.4	$4.13 \cdot 10^{36}$		
140	231.3	13 25 21.8	-43 04 51.2	120	70.1	$7.33 \cdot 10^{36}$		
141	233.2	13 25 12.0	-42 58 30.7	63	33.6	$3.02 \cdot 10^{36}$		
142	234.6	13 25 12.3	-42 58 24.6	82	56.4	$5.12 \cdot 10^{36}$		
143	234.7	13 25 47.2	-43 02 43.6	181	151.7	$1.32 \cdot 10^{37}$		
144	235.4	13 25 14.8	-43 04 18.0	89	35.8	$3.89 \cdot 10^{36}$		
145	237.9	13 25 38.9	-43 04 32.1	32	17.5	$1.63 \cdot 10^{36}$		
146	238.4	13 25 22.4	-42 57 17.4	914	845.7	$7.37 \cdot 10^{37}$	GC	mrfa-208
147	239.1	13 25 46.4	-43 03 10.8	406	356.8	$3.35 \cdot 10^{37}$	FS	mrfa-93
148	239.7	13 25 09.2	-42 58 59.5	682	594	$5.21 \cdot 10^{37}$	GC	mrfa-215
149	244.4	13 25 06.3	-43 02 21.2	974	818.5	$8.26 \cdot 10^{37}$		
150	245.6	13 25 15.8	-42 57 39.9	141	106.5	$9.78 \cdot 10^{36}$		
151	248.9	13 25 05.0	-43 01 33.5	292	239.9	$2.51 \cdot 10^{37}$		
152	249.9	13 25 34.3	-42 57 09.7	47	25.2	$2.46 \cdot 10^{36}$		
153	252.6	13 25 47.6	-42 59 03.8	56	36.4	$3.31 \cdot 10^{36}$		
154	253.4	13 25 29.2	-43 05 21.5	32	19.4	$3.10 \cdot 10^{36}$		
155	254.6	13 25 48.6	-43 02 58.4	33	18.8	$2.02 \cdot 10^{36}$		
156	256.5	13 25 27.6	-43 05 25.3	55	37.2	$4.92 \cdot 10^{36}$		
157	258.0	13 25 38.6	-42 57 20.5	102	57.5	$5.36 \cdot 10^{36}$		
158	258.7	13 25 18.9	-42 57 08.5	91	61.5	$6.02 \cdot 10^{36}$		
159	260.7	13 25 23.5	-42 56 52.0	204	170.4	$1.78 \cdot 10^{37}$		
160	261.5	13 25 04.4	-43 00 08.2	94	69.8	$7.71 \cdot 10^{36}$		
161	261.7	13 25 45.5	-42 58 15.9	242	179.5	$1.73 \cdot 10^{37}$		
162	265.1	13 25 33.7	-43 05 25.4	86	63.8	$8.22 \cdot 10^{36}$	FS	HD 116647 fs
163	265.6	13 25 48.5	-43 03 22.8	56	41.8	$5.83 \cdot 10^{36}$		
164	268.9	13 25 39.8	-43 05 01.9	100	86.8	$2.20 \cdot 10^{37}$	GC	pff-gc-111
165	270.0	13 25 47.2	-42 58 25.6	179	139.7	$1.22 \cdot 10^{37}$		
166	270.4	13 25 38.1	-43 05 13.6	98	82.2	$2.00 \cdot 10^{37}$		
167	272.5	13 25 26.2	-42 56 36.7	184	139.6	$1.25 \cdot 10^{37}$		
168	273.2	13 25 49.5	-42 58 58.4	34	16.6	$1.62 \cdot 10^{36}$		
169	273.3	13 25 35.2	-43 05 29.0	18	14.2	$4.67 \cdot 10^{36}$	GC	whh-17
170	281.1	13 25 27.6	-43 05 49.9	59	35.1	$4.60 \cdot 10^{36}$		
171	282.5	13 25 03.5	-42 59 28.8	29	17.2	$2.36 \cdot 10^{36}$		
172	284.3	13 25 39.1	-42 56 54.0	352	297.3	$2.67 \cdot 10^{37}$		
173	285.5	13 25 07.5	-43 04 09.3	6878	6474.7	$6.69 \cdot 10^{38}$	FS	Kraft
174	285.7	13 25 53.6	-43 01 34.9	73	44.4	$3.95 \cdot 10^{36}$		
175	287.1	13 25 46.7	-42 57 52.6	90	40.5	$3.51 \cdot 10^{36}$		
176	289.0	13 25 02.7	-43 02 43.5	2412	2257.9	$2.45 \cdot 10^{38}$		

Table A.1. continued.

ID (1)	Dist (2)	R.A. (3)	Dec. (4)	Total Cts (5)	Source Cts (6)	Luminosity (7)	Type (8)	ID reference (9)
177	290.1	13 25 32.8	-42 56 24.2	165	115.8	$1.01 \cdot 10^{37}$	GC	pff-gc-056
178	291.2	13 25 12.0	-42 57 13.3	29	21.9	$9.13 \cdot 10^{36}$		
179	301.8	13 25 55.1	-43 01 19.2	198	153.7	$1.31 \cdot 10^{37}$		
180	302.2	13 25 38.4	-42 56 30.8	150	100.3	$8.94 \cdot 10^{36}$		
181	304.3	13 25 20.3	-42 56 15.4	42	32.2	$1.02 \cdot 10^{37}$		
182	312.9	13 25 52.2	-42 58 30.7	71	21.6	$1.86 \cdot 10^{36}$	GC	pff-gc-072
183	313.4	13 25 54.6	-42 59 25.8	1500	1311.5	$1.10 \cdot 10^{38}$	GC	pff-gc-131
184	315.7	13 25 49.8	-43 04 30.3	26	18.5	$5.02 \cdot 10^{36}$		
185	321.8	13 25 56.9	-43 00 44.8	319	244.3	$2.07 \cdot 10^{37}$		
186	321.8	13 25 46.6	-42 57 03.4	638	487.2	$4.56 \cdot 10^{37}$	GC	pff-gc-168
187	321.9	13 25 49.2	-43 04 47.3	60	37.2	$8.91 \cdot 10^{36}$		
188	322.2	13 25 08.3	-43 05 11.3	364	189.8	$2.11 \cdot 10^{37}$		
189	327.5	13 25 09.6	-43 05 29.6	538	418.6	$4.66 \cdot 10^{37}$		
190	327.6	13 25 34.5	-42 55 49.9	239	164.9	$1.48 \cdot 10^{37}$		
191	336.0	13 25 18.6	-42 55 47.8	10	6.4	$3.11 \cdot 10^{36}$		
192	336.9	13 25 53.4	-42 58 06.5	106	40.4	$3.50 \cdot 10^{36}$		
193	338.8	13 25 12.9	-43 06 06.6	43	25.1	$3.07 \cdot 10^{36}$		
194	339.5	13 25 47.4	-42 56 47.4	144	70.8	$6.87 \cdot 10^{36}$		
195	347.6	13 25 39.4	-42 55 46.3	94	38.9	$3.44 \cdot 10^{36}$		
196	350.1	13 25 43.9	-43 06 10.0	146	132.4	$5.91 \cdot 10^{37}$		
197	353.6	13 25 07.7	-42 56 30.5	70	56.3	$2.80 \cdot 10^{37}$	GC	mrfa-216
198	356.5	13 25 10.2	-42 56 08.1	39	30.2	$1.61 \cdot 10^{37}$		
199	360.4	13 25 45.2	-42 56 04.5	95	31	$2.90 \cdot 10^{36}$		
200	362.3	13 24 56.1	-43 02 59.0	144	80.9	$1.09 \cdot 10^{37}$		
201	364.8	13 25 57.2	-42 58 22.3	414	291.8	$3.12 \cdot 10^{37}$		
202	366.3	13 25 10.7	-43 06 24.5	398	299.5	$3.28 \cdot 10^{37}$		
203	370.6	13 25 22.7	-42 55 02.1	109	92	$4.22 \cdot 10^{37}$		
204	372.3	13 26 01.5	-43 00 43.5	109	37.9	$3.32 \cdot 10^{36}$		
205	374.0	13 25 54.6	-42 57 20.8	38	16.1	$2.15 \cdot 10^{36}$		
206	374.2	13 25 31.4	-43 07 20.7	33	26.6	$1.24 \cdot 10^{37}$		
207	381.9	13 25 29.2	-42 54 47.3	22	15.5	$6.89 \cdot 10^{36}$		
208	389.6	13 25 45.2	-42 55 30.6	96	36.9	$3.92 \cdot 10^{36}$		
209	389.6	13 25 52.6	-43 05 45.5	45	38.1	$1.79 \cdot 10^{37}$	GC	pff-gc-129
210	390.5	13 25 03.1	-42 56 25.5	43	29	$1.43 \cdot 10^{37}$	GC	pff-gc-157
211	393.1	13 25 57.2	-43 04 50.5	68	44.2	$1.05 \cdot 10^{37}$		
212	395.6	13 25 58.7	-43 04 30.4	1259	1180.4	$2.69 \cdot 10^{38}$		
213	396.1	13 25 10.1	-43 06 55.1	137	90.2	$1.22 \cdot 10^{37}$		
214	396.2	13 25 29.0	-43 07 44.7	23	16.5	$7.34 \cdot 10^{36}$		
215	397.9	13 25 49.7	-43 06 24.7	18	10.5	$4.58 \cdot 10^{36}$		
216	405.4	13 25 10.3	-42 55 10.8	80	65	$3.34 \cdot 10^{37}$		
217	405.7	13 25 14.0	-43 07 25.9	222	168.2	$2.72 \cdot 10^{37}$		
218	409.8	13 25 48.8	-42 55 31.0	76	47.7	$1.05 \cdot 10^{37}$		
219	413.6	13 25 57.9	-42 57 02.5	393	296.1	$4.21 \cdot 10^{37}$		
220	420.9	13 25 21.3	-42 54 13.7	113	98.8	$4.82 \cdot 10^{37}$		
221	424.8	13 26 06.4	-43 01 12.3	35	19.7	$5.82 \cdot 10^{36}$		
222	424.9	13 25 45.4	-42 54 51.4	119	80.3	$1.69 \cdot 10^{37}$		
223	426.3	13 25 33.2	-43 08 10.6	38	28.1	$1.25 \cdot 10^{37}$		
224	436.7	13 25 22.7	-43 08 22.2	20	13.3	$6.24 \cdot 10^{36}$		
225	443.8	13 25 01.1	-43 06 43.8	971	853	$1.16 \cdot 10^{38}$		
226	445.1	13 25 11.2	-43 07 55.9	144	101.4	$1.48 \cdot 10^{37}$		
227	449.7	13 25 06.8	-43 07 36.5	86	43.1	$6.10 \cdot 10^{36}$		
228	450.3	13 26 01.2	-43 05 28.0	949	919.9	$4.14 \cdot 10^{38}$		
229	453.4	13 25 44.1	-43 08 04.5	146	135.7	$6.92 \cdot 10^{37}$		
230	453.7	13 25 40.5	-43 08 20.1	18	11	$5.37 \cdot 10^{36}$		
231	460.3	13 25 50.3	-42 54 41.9	82	34.4	$4.82 \cdot 10^{36}$		
232	462.6	13 24 59.0	-43 06 48.9	74	34.9	$4.96 \cdot 10^{36}$		
233	464.9	13 24 50.4	-43 04 52.3	106	55.9	$7.67 \cdot 10^{36}$		
234	470.6	13 25 57.5	-42 55 31.5	73	38.2	$5.28 \cdot 10^{36}$		
235	474.2	13 25 04.0	-42 54 31.5	107	44.1	$6.57 \cdot 10^{36}$		

Table A.1. continued.

ID (1)	Dist (2)	R.A. (3)	Dec. (4)	Total Cts (5)	Source Cts (6)	Luminosity (7)	Type (8)	ID reference (9)
236	479.6	13 26 09.9	-43 03 10.5	32	17.3	$4.32 \cdot 10^{36}$		
237	479.6	13 25 57.5	-43 06 59.2	23	16.7	$8.07 \cdot 10^{36}$		
238	481.3	13 25 13.9	-42 53 31.5	344	283.6	$4.18 \cdot 10^{37}$		
239	483.9	13 25 48.1	-43 08 17.2	43	29.7	$1.35 \cdot 10^{37}$		
240	488.6	13 25 11.3	-43 08 43.5	51	34.2	$1.11 \cdot 10^{37}$		
241	491.9	13 25 42.0	-42 53 23.1	26	16.6	$8.55 \cdot 10^{36}$		
242	493.4	13 25 10.4	-42 53 33.2	415	334.4	$4.92 \cdot 10^{37}$		
243	494.0	13 26 11.9	-43 02 42.9	280	247	$6.45 \cdot 10^{37}$		
244	494.1	13 25 35.2	-42 53 01.7	246	233.2	$1.04 \cdot 10^{38}$		
245	495.2	13 25 46.7	-42 53 40.1	209	118.5	$1.64 \cdot 10^{37}$		
246	496.3	13 25 02.9	-42 54 13.2	307	211.7	$3.10 \cdot 10^{37}$		
247	499.4	13 26 05.5	-42 56 32.5	191	132.7	$1.89 \cdot 10^{37}$	GC	pff-gc-122
248	500.7	13 25 55.5	-43 07 45.8	29	20.6	$9.29 \cdot 10^{36}$		
249	513.4	13 26 14.1	-43 02 08.6	73	55.6	$2.84 \cdot 10^{37}$		
250	523.7	13 25 11.0	-42 52 57.8	50	26.5	$4.44 \cdot 10^{36}$		
251	524.3	13 25 27.3	-43 09 53.1	61	48	$2.21 \cdot 10^{37}$		
252	542.7	13 24 58.9	-43 08 31.3	167	86.8	$1.33 \cdot 10^{37}$		
253	543.0	13 24 56.8	-43 08 13.7	798	594.6	$8.36 \cdot 10^{37}$		
254	543.6	13 25 39.2	-43 09 57.3	38	24.9	$1.15 \cdot 10^{37}$		
255	548.4	13 26 15.9	-42 58 46.8	530	392.4	$4.70 \cdot 10^{37}$		
256	549.4	13 25 46.5	-43 09 38.0	119	102.7	$4.67 \cdot 10^{37}$		
257	553.0	13 24 50.5	-43 07 22.9	271	151.4	$2.17 \cdot 10^{37}$		
258	553.8	13 25 57.5	-42 53 42.2	282	136.4	$1.52 \cdot 10^{37}$	FS	GF Blue 1
259	556.4	13 25 26.0	-42 51 52.7	160	96.2	$1.44 \cdot 10^{37}$		
260	560.6	13 25 49.3	-42 52 41.4	897	757.4	$1.55 \cdot 10^{38}$		
261	563.6	13 25 03.1	-43 09 24.3	163	85.2	$1.28 \cdot 10^{37}$		
262	564.4	13 25 11.0	-42 52 14.8	109	56.3	$9.01 \cdot 10^{36}$		
263	565.8	13 25 34.0	-43 10 30.2	46	34.5	$1.61 \cdot 10^{37}$		
264	569.9	13 26 13.1	-42 56 32.9	142	68.8	$7.77 \cdot 10^{36}$		
265	585.6	13 26 20.5	-42 59 47.2	142	78.6	$1.94 \cdot 10^{37}$		
266	586.0	13 26 19.7	-43 03 18.8	75	52.7	$2.60 \cdot 10^{37}$		
267	588.5	13 24 54.4	-42 53 26.8	65	35.2	$7.91 \cdot 10^{36}$		
268	592.0	13 25 41.7	-42 51 37.4	24	18	$8.28 \cdot 10^{36}$		
269	593.6	13 25 41.9	-43 10 41.4	642	610.1	$2.86 \cdot 10^{38}$	GC	pff-gc-188
270	595.8	13 25 44.3	-42 51 41.7	18	12.9	$5.96 \cdot 10^{36}$		
271	597.4	13 25 48.5	-42 51 56.9	25	20.8	$9.54 \cdot 10^{36}$		
272	597.7	13 25 31.0	-43 11 05.3	152	139.1	$7.25 \cdot 10^{37}$	GAL	pff-qso-6

(1) – the sequence number; (2) – distance from the center in arcsec; (3),(4) – right ascension and declination, J2000; (5) – total number of counts in the `wavdetect` source cell, source+background; (6) – number of source counts after background subtraction (7) – X-ray luminosity, 0.5–8 keV, assuming 3.5 kpc distance; (7) – source type: GC – confirmed globular cluster, FS – foreground star, GAL – background galaxy, H_α – H_α emitter; (7) – precise identification and reference: pff – Peng et al. (2004), Tables 5 and 9; mrfa – Minniti et al. (2003), Tables 1 and 3; whh – Woodley et al. (2005) Tables 1 and 2 ; GF – Graham & Fasset (2002) Table 1; Kraft – Kraft et al. (2001) Sect. 5.1; HD – Roeser et al. (1991).

Comments: Source #121 was designated a globular cluster by Minniti et al. (2003), but according to Woodley et al. (2005) it is a background galaxy; Minniti et al. (2003) claim to have removed sources with H_α -emission from their list of globular clusters. However two sources (#54 and #108 in our source list) are both listed as H_α -emitters and globular clusters in their tables. We assume that they are H_α sources and designate them accordingly. Sources #146, #148 and #197 are included in the list of globular clusters of Minniti et al. (2003), although no colours are available. They are marked as globular cluster in the Table.